Journal of Nuclear Materials 552 (2021) 153006

Contents lists available at ScienceDirect

Journal of Nuclear Materials

journal homepage: www.elsevier.com/locate/jnucmat

Microstructure investigations of $Fe_{50}Mn_{30}Co_{10}Cr_{10}$ dual–phase high–entropy alloy under Fe ions irradiation

Ji Wang[a], Jianlong Chai[b], Hongpeng Zhang[b], Pengfei Tai[b], Chao Liu[b], Lijuan Niu[b], Wenhao He[c], Weiying Huang[d], Rui Shu[e], Laihui Luo[a], Weiping Li[a], Yabin Zhu[b,*], Cunfeng Yao[b,*], Peifeng Gao[f,*]

[a] School of Physical Science and Technology, Ningbo University, Ningbo, 315211, China
[b] Institute of Modern Physics, Chinese Academy of Sciences, Lanzhou, 730000, China
[c] Key Laboratory of Solid Lubrication, Lanzhou Institute of Chemical Physics, Chinese Academy of Sciences, Lanzhou, 730000, China
[d] School of Energy and Power Engineering, Changsha University of Science and Technology, Changsha, 410114, China
[e] Thin Film Physics Division, Department of Physics, Chemistry, and Biology (IFM), Linköping University, Linköping, Sweden
[f] Key Laboratory of Mechanics on Western Disaster and Environment, Ministry of Education, College of Civil Engineering and Mechanics, Lanzhou University, Lanzhou, 730000, China

ARTICLE INFO

Article history:
Received 9 February 2021
Revised 18 March 2021
Accepted 6 April 2021
Available online 20 April 2021

Keywords:
High–entropy alloy
Irradiation
TEM
Twinning–induced plasticity
Transformation–induced plasticity

ABSTRACT

An $Fe_{50}Mn_{30}Co_{10}Cr_{10}$ dual–phase high–entropy alloy (DP–HEA) was irradiated at room temperature with 3 MeV Fe ions to a dose of 50 displacement per atom (dpa) . Potentials of special elemental designed DP–HEAs with low stacking fault energy (SFE) as promising candidate materials for future nuclear energy systems are evaluated. Transmission electron microscopy (TEM) analysis finds that FCC γ–γ, HCP ε–ε twinning structures and FCC γ–HCP ε co-existed structures of the DP–HEA, which correlate with the combined high strength and high ductility featured by this alloy, remain stable under a displacement damage of 50 dpa. No elemental segregation after irradiation was detected by energy dispersive spectroscopy. The results indicate that TWIP and TRIP mechanisms, owned by many other DP–HEAs, may still work effectively, and the materials still possess the merits of combined high strength and ductility brought by TWIP and TRIP mechanisms under irradiation conditions. Defects free channels (DFCs) and abundant Lomer–Cottrell (L–C) locks are observed in the irradiated samples after tensile deformation. The immobile L–C locks restrict DFCs growth, prevent the pile-up of dislocation along grain boundaries, thus sustaining dislocations in the grain interior. This study provides a new strategy to improve simultaneously the irradiation resistance and mechanical properties of structural materials by introducing the TWIP and TRIP mechanisms.

1. Introduction

Enhancing irradiation resistant property of promising candidate materials while keeping or improving mechanical property simultaneously is an essential requirement for the improvement of safety and life expectancies of the future nuclear energy systems. During the past decades, R&D of new structural materials with improved irradiation resistance has made a great progress. Among the many promising candidate materials developed in recent years, high–entropy alloys (HEAs) or multicomponent alloys have attracted considerable attention due to their excellent mechanical properties, good corrosion resistance and high temperature oxidization resistance [1–3]. A number of recent studies have been focused on the irradiation tolerance of HEAs [4–11]. Different from traditional ways that suppressing the irradiation induced damage and improving the irradiation resistance of alloys by increasing the sink density (e.g. grain boundaries, dislocations, second phase particle interfaces, etc.) [12,13], HEAs show a unique irradiation resistant behavior due to special chemical composition and microstructural characters. For example, Granberg et al. found that increasing compositional elements reduces dislocation mobility in the NiCoCr alloys, improves phase stability, and results in a substantial reduction of damage accumulation under prolonged irradiation condition [5]. Lu et al. studied a series of NiCoFeCrMn multicomponent alloys and found that enhanced point defect recombination is achieved when interstitial defect cluster motion

* Corresponding authors.
E-mail addresses: zhuyabin@impcas.ac.cn (Y. Zhu), ycf@impcas.ac.cn (C. Yao), gaopf@lzu.edu.cn (P. Gao).

https://doi.org/10.1016/j.jnucmat.2021.153006
0022-3115/

changes from a long–range one–dimensional mode to a short–range three–dimensional mode by increasing the compositional elements [6].

However, most of the studies have been devoted to the irradiation behavior of single–phase HEAs, rather than dual–phase HEAs (DP–HEAs) . Unlike most other conventional alloys that display a strength–ductility trade–off, specific chemical composition–designed DP–HEAs with low stacking fault energy (SFE) show a simultaneous increase of strengthen and ductility, and display excellent mechanical properties [14,15]. This character makes the DP–HEAs worthy to be investigated as potential candidate materials for future nuclear systems. Except the consideration of irradiation effects, structural materials served in the future nuclear systems undergo a large external mechanical load, which could result in material deformation and induce significant twinning–induced plasticity (TWIP) mechanism and transformation–induced plasticity (TRIP) mechanism of the DP–HEAs. It is reported that the excellent strength–ductility combination of the DP–HEAs originates from the TWIP and TRIP mechanisms [15]. Therefore, the availability of TWIP and TRIP mechanisms and the stability of microstructure induced by TWIP and TRIP mechanisms under irradiation condition are crucial for the irradiation resistant properties of DP–HEAs. However, seldom work has been reported on this subject.

$Fe_{50}Mn_{30}Co_{10}Cr_{10}$ alloy is a typical DP–HEA consisting of ε phase with an HCP atomic arrangement structure and γ phase with an FCC atomic arrangement structure. Due to the low SFE (6.5 mJ m^{-2}) [14], when external mechanical load induces material deformation, multiple twinning structures occur (TWIP effect) . Moreover, a dynamic forward (FCC $\gamma \rightarrow$ HCP ε) and backward (HCP $\varepsilon \rightarrow$ FCC γ) phase transformation initiate (denoted as bidirectional transformation induced plasticity, B–TRIP effect), and during this dynamic transformation process, the grain is continuously self–refining down to a few nanometers [14]. The special microstructural evolution of this DP–HEA material under mechanical loads makes it interesting and worthy to be chosen as a model DP–HEAs system to investigate whether the microstructure induced by the TWIP and B–TRIP effects remain effective in improving the mechanical properties and the availability of TWIP and TRIP mechanisms under irradiation condition as it is required in nuclear reactors.

In this study, the $Fe_{50}Mn_{30}Co_{10}Cr_{10}$ DP–HEA was chosen as the material to be studied not for any specific application in nuclear systems, but to take advantage of its TWIP and B–TRIP effects to evaluate qualification of DP-HEAs as potential candidate materials for future nuclear materials. On one hand, Fe ions irradiation were employed on the tensile DP–HEAs to investigate its structural stability. On the other hand, tensile deformation was applied on the irradiated samples to study the microstructural evolution when irradiation induced defects are present. It is found that, the γ–γ, ε–ε twinning structure and γ–ε co–existed structures, which is responsible for the high strength and high ductility, remain stable at a displacement damage of 50 dpa. Moreover, no element segregation was detected after irradiation. The size of defect free channels (DFCs) in the irradiation and tensile conditions were restricted, showing a good working hardening capability. The results show a good irradiation tolerance of the DP–HEAs and the validity of TWIP and B–TRIP mechanisms under irradiation condition, and indicate the potential application of DP–HEAs as the candidate materials in nuclear energy systems.

2. Experimental procedure

2.1. Materials preparation

The material used in this study is a type of DP–HEA, the nominal chemical composition is $Fe_{50}Mn_{30}Co_{10}Cr_{10}$, where the subscripts are atomic percent. The HEA was synthesized by vacuum–levitation melting in a high–purity Ar atmosphere. The ingots were remelted at least three times to achieve a homogeneous distribution of elements and then recrystallized at 1200 °C for 2 hours followed by water–quenching. Rectangular dog–bone–shaped samples with a thickness of 1.5 mm, a gauge length of 9 mm and a width of 2 mm was fabricated by electrical discharge machining. Before irradiation, the dog–bone–shaped samples were mechanically polished using silicon carbide abrasive paper until the mirror–like surface formed and then electrochemically polished to remove the residual stress.

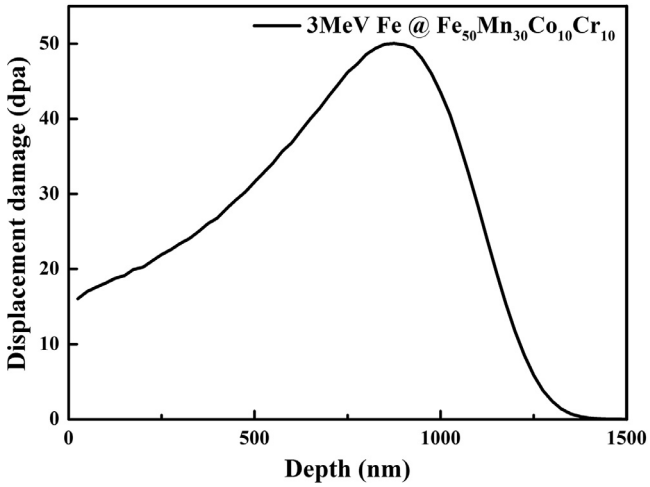

Fig. 1. Displacement damage as a function of depth for $Fe_{50}Mn_{30}Co_{10}Cr_{10}$ DP–HEA irradiated with 3–MeV Fe ions.

2.2. Irradiation and tensile deformation

The ion irradiation experiments were carried out at room temperature (RT) under a vacuum pressure of 10^{-5} Pa in a terminal chamber of the 320 kV multi–discipline research platform for highly charged ions at the Institute of Modern Physics, Chinese Academy of Science. The samples were pasted on a large block of stainless steel by silver conductive adhesive, the temperature was monitored by an infrared thermometer, and the temperature was kept below 50 °C during the irradiation experiment. 3 MeV Fe^{13+} ions were employed to irradiate the samples to a displacement of 50 dpa at the Bragg peak depth. The displacement damage induced by energetic Fe ions was simulated by SRIM code using the "Kinchin–Pease quick calculation" mode, and the displacement damage profile is shown in Fig. 1. Tensile deformation (MTS, E43. 104) was performed at an engineering strain rate of 10^{-3} s^{-1} to an engineering strain of 34%. Two sets of samples need to be distinguished. For the first set of samples, tensile deformation was performed prior to the irradiation procedure (denoted as T–I samples) . For the second set of samples, the irradiation procedure was carried out prior to the tensile deformation (denoted as I–T samples) .

2.3. Characterization methods

The grain orientation, grain size and phase distribution of the specimens were characterized by Scanning Electron Microscopy (SEM) equipped with an electron backscatter diffraction detector (EBSD, FEI–Quanta–FEG–250) . The EBSD data was analyzed using a TSL OIM data-analysis software. Focused Ion Beam (FIB, Helios–G4–CX) technique was employed to lift out the thin film for TEM analysis. Transmission electron microscopy (TEM, Talos F200x) op-

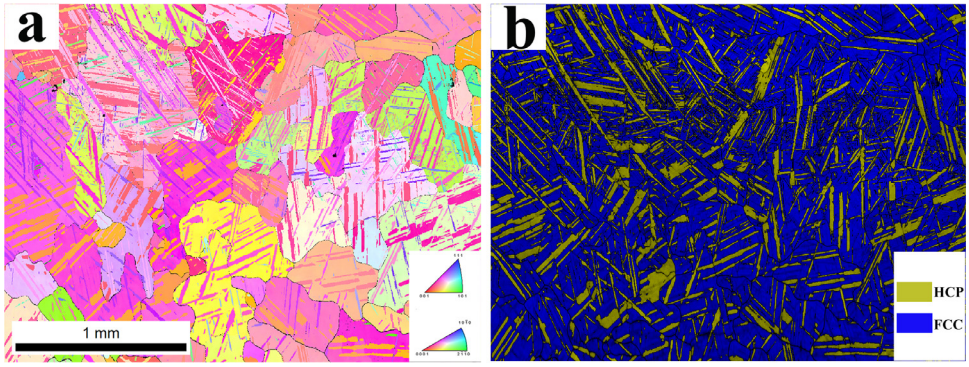

Fig. 2. EBSD maps of the virgin $Fe_{50}Mn_{30}Co_{10}Cr_{10}$ DP–HEA. (a) Orientation imaging microscopy. (b) Distribution of FCC γ phase and HCP ε phase.

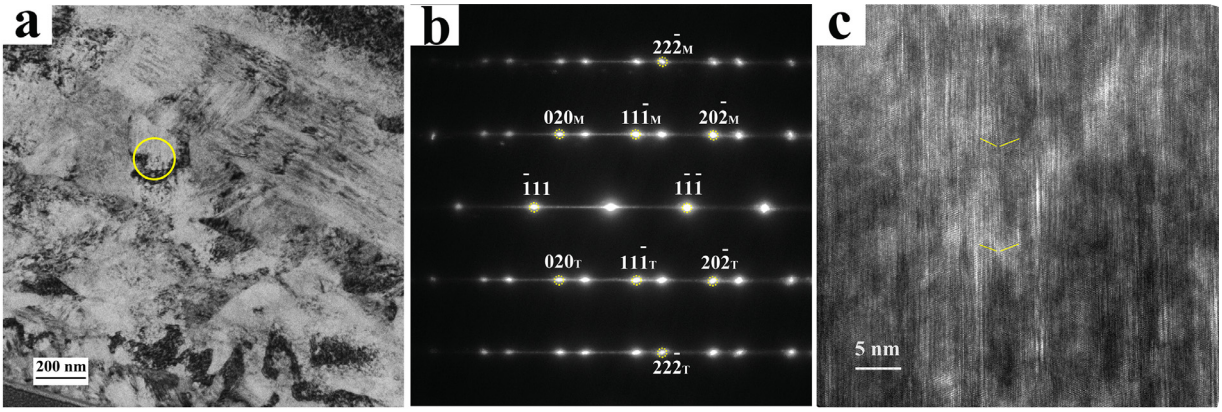

Fig. 3. Microstructure of γ–γ twinning structure in T–I sample. (a) Bright-field TEM image acquired from the T–I sample. (b) SAED pattern acquired from the yellow circle region labeled in (a) . (c) HRTEM image acquired from the yellow circle region of (a). (For interpretation of the references to color in this figure legend, the reader is referred to the web version of this article.)

erating at 200 kV was used for the microstructural characterization of the cross–sectional TEM specimens.

3. Results

3.1. Microstructure of virgin $Fe_{50}Mn_{30}Co_{10}Cr_{10}$ sample

Fig. 2 shows representative EBSD maps of the virgin $Fe_{50}Mn_{30}Co_{10}Cr_{10}$ DP–HEA. The crystallographic orientations and grain size in Fig. 2a are clearly observed. The DP–HEA consists of FCC γ phase (blue in Fig. 2b) and HCP ε phase laminate layers (yellow in Fig. 2b) with a volume fraction of 73 % and 27%, respectively. The grain size of γ matrix ranges from tens of micrometers to a millimeter and the thickness of ε phase laminate layers range from hundreds of nanometers to tens of micrometers according to the image resolution.

3.2. Microstructure of the T–I and I–T samples

Fig. 3 shows the TEM images of microstructural morphology for the T–I sample. From the phase contrast in the low–magnification TEM image of Fig. 3a, it can be observed that twinning structures are prominent in the DP–HEAs. Fig. 3b shows a selected area diffraction (SAED) pattern recorded along [110] FCC zone axis at the displacement damage peak position (labeled as the yellow circle region in Fig. 3a) . The elongated diffraction spots indicate the existence of stacking faults, and only diffraction spots belonging to FCC γ–γ twinning structure were found in this area. To reveal the detail microstructural feature, a HRTEM image was acquired along the [110] FCC zone axis at the same region (Fig. 3c) . It demonstrates clearly the existence of nanoscale twinning structure and a high–density of stacking faults in the {111} close–packed planes.

Fig. 4 are the TEM images acquired from another region of the same sample. Fig. 4b is the corresponding SAED pattern from the yellow circle region in Fig. 4a. Two sets of diffraction patterns belonging to ε–ε twinning structures are indexed. The SAED pattern indicates that the electron beam was along the $[11\bar{2}0]$ zone axes of the ε phase and the diffraction patterns share the same diffraction spot (i.e. $(1\bar{1}02)$) . To reveal the microstructural nature of the selected area, a corresponding HRTEM image is shown in Fig. 4c, from which a ε–ε $\{10\bar{1}2\}$ twin boundary (TB) can be clearly seen. Along the TB, two different microstructures coexist, i.e. $\{10\bar{1}2\}$ coherent ε–ε twin boundaries and pervasively existed basal/prismatic (BP) or prismatic/basal (PB) steps. These steps are formed by the basal planes of the γ–parent grains and the prismatic planes of the ε–twin grains, which are energetically favorable and geometrically necessary for the migration of twin boundaries [16,17].

Fig. 5a shows the low–magnification cross–sectional TEM images of T–I sample. In this region of the sample, lath structures intersecting with each other are prominent. A detail characterization shows that the lath grains are a mixture of γ and ε phases. Fig. 5b displays the SAED pattern acquired from the peak irradiation damage position labeled as the yellow circle in Fig. 5a. Two sets of diffraction spots are indexed, i.e. the diffraction pattern along the [110] zone axis of γ phase and the diffraction pattern along the $[11\bar{2}0]$ zone axis of ε phase. The SAED confirms a good consistence of S–N relationship between γ phase and ε phase (i.e. $<110>\gamma//<11\bar{2}0>\varepsilon$.), which are in agreement with previous report [18]. Fig. 5c presents a HRTEM image taken along the [110] direc-

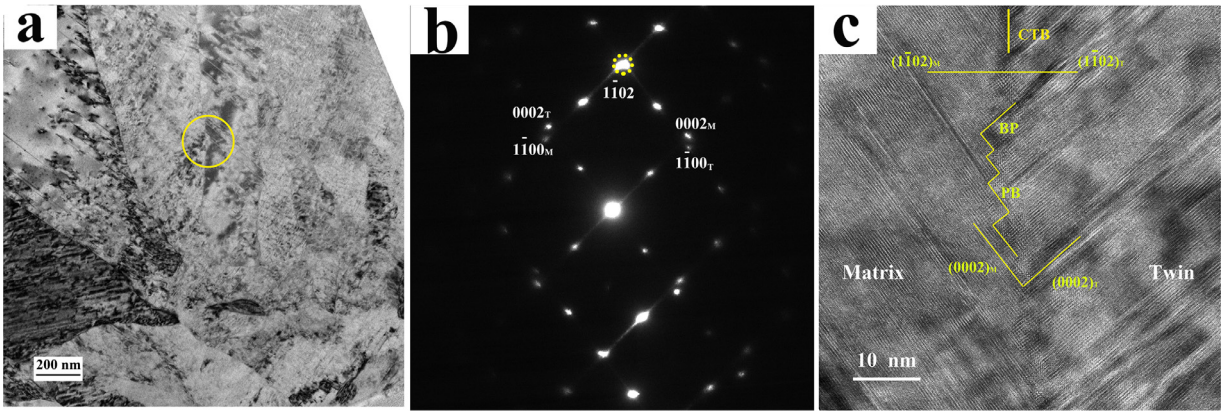

Fig. 4. Microstructure of ε–ε twinning structure in T–I sample. (a) Bright-field TEM image acquired from the T–I sample. (b) SAED pattern from the yellow circle region labeled in (a) . (c) HRTEM image acquired from the yellow circle region of (a). (For interpretation of the references to color in this figure legend, the reader is referred to the web version of this article.)

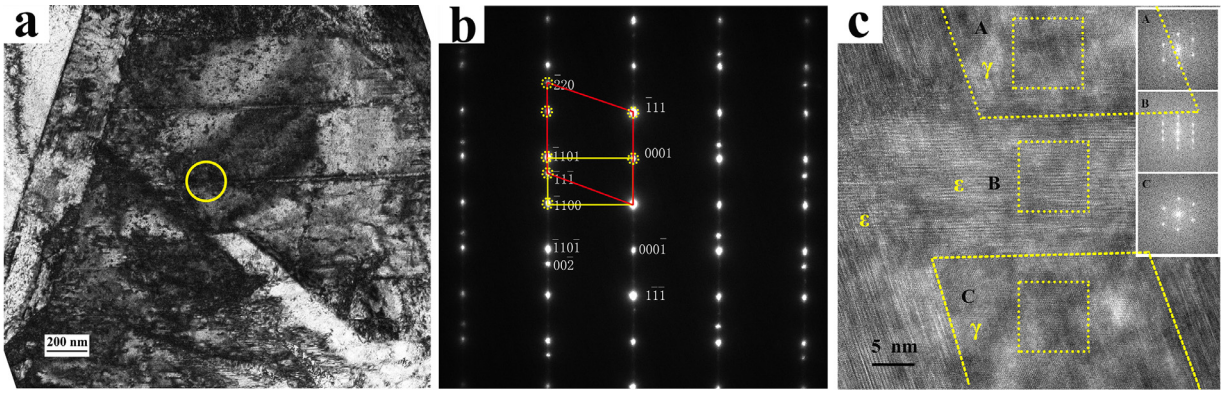

Fig. 5. Orientation relationship of γ–ε phase in T–I sample. (a) Bright-field TEM image shows the general microstructural feature. (b) Corresponding SAED pattern from the yellow circle region of (a) showing a S-N relationship between γ and ε phase. (c) HRTEM image acquired from the yellow circle region of (a). (For interpretation of the references to color in this figure legend, the reader is referred to the web version of this article.)

tion of the γ phase from the yellow circle region of Fig. 5a, and insets are the corresponding fast Fourier transform (FFT) patterns from the corresponding square boxes labeled as A, B and C, respectively. It shows that the γ phases (region A and C) and ε phase (region B) co–existed after the irradiation, and the nanolaminate is on the order of tens of nanometers, which have been reported that within this length scale, the compositional phases can improve greatly both strength and ductility [14]. No diffuse scattering rings, and only diffraction patterns belong to γ–γ twinning structure, ε–ε twinning structure and γ–ε structure are detected from the SAED patterns in Figs. 3b, 4b and 5b, respectively, indicating that no amorphization, no phase decomposition or incoherent precipitation were observed after irradiation.

Fig. 6 shows another set of TEM images recording the microstructure of I–T sample. The bright–field TEM image of Fig. 6a shows an overview of the microstructural characteristics. A specific feature should be noted is that the regions with white contrast marked by the yellow arrows are free of defects. To highlight the regions, a dark–field TEM image obtained using one of the {111} reflections of the γ phase is presented in Fig. 6b. This specific morphology was observed in other irradiated alloys after tensile deformation, and is termed as defect–free channels (DFCs) [19–21]. By tilting the TEM thin film, no defect clusters were observed in the DFCs, thus proving that the DFCs recorded in this study were formed by perfect dislocations rather than twins. Incidentally, no DFCs were detected in the T-I sample. A HRTEM image acquired from the [110] zone axis of the γ phase in rectangle A is presented in Fig. 6c. As it is shown, two sets of stacking faults (distribute in the (111) and $(1\bar{1}\bar{1})$ close–packed planes, respectively) can be clearly seen, the angle between the two sets of stacking faults is close to 70°. This is consistent with the angle between the close–packed planes {111} in the FCC crystal structures, e.g. between (111) close–packed plane and $(1\bar{1}\bar{1})$ close–packed plane. Moreover, the stacking faults reacted with each other, and formed a Lomer–Cottrell lock (L–C lock), shown as the dash yellow circle in HRTEM image (Fig. 6c) . The L–C locks locate at the edges of DFCs and restrict the size of DFCs.

4. Discussion

4.1. Microstructural stability

The presence of a TB causes the local change of atomic stacking sequence between the parent lattice and the twin lattice, results in an extra energy for the transmission of dislocations across the TBs [22,23], thereby increases the strength of materials. Twinning on the {111} plane is frequently observed in FCC crystal structures, and in HCP alloys, twinning on the $\{10\bar{1}n\}$ and $\{11\bar{2}n\}$ planes (n = 1, 2, 3, 4) are commonly reported [24]. Recent research shows that TBs are efficient in alleviating radiation–induced damage by serving as defect sinks to trap and annihilate radiation–induced defects [25,26]. In this study, due to the extremely low stacking fault energy (6.5 mJ m^{-2}) of $Fe_{50}Mn_{30}Co_{10}Cr_{10}$ DP–HEA [14], twinning is a predominant microstructural evolution mechanism induced by tensile deformation. For the FCC crystal structure, twinning structure includes coherent twin boundaries $\sum^3\{111\}$ (CTBs) without appar-

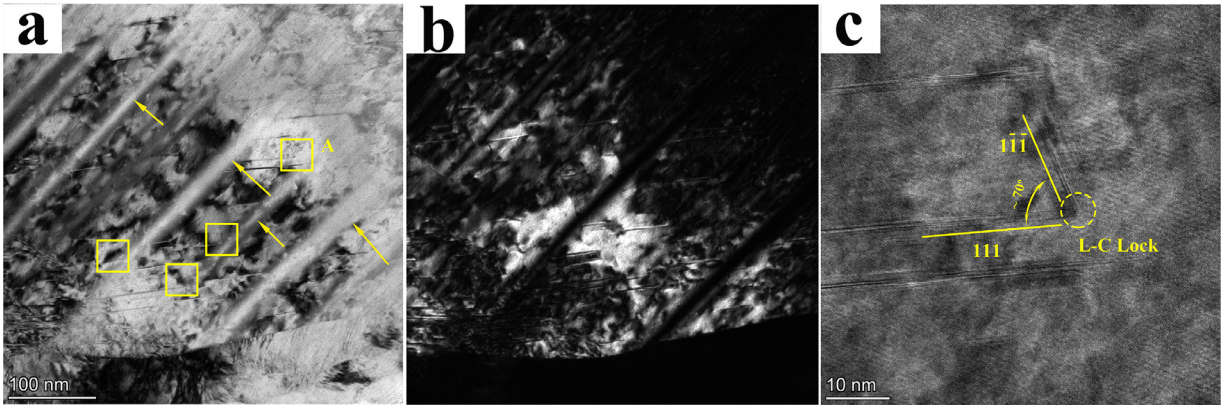

Fig. 6. Microstructure of the I–T sample. (a) Low magnification bright-field TEM image shows the morphology of DFCs (indicated by the yellow arrows) . (b) Corresponding dark-field TEM image of (a) . (c) HRTEM image shows the microstructure of a L–C lock. (For interpretation of the references to color in this figure legend, the reader is referred to the web version of this article.)

ent free volume and incoherent twin boundaries $\sum^3\{112\}$ (ITBs) with Shockley partial dislocations [23]. Under irradiation conditions, abundant point defects are produced and aggregate into clusters, these defects interact with CTBs, and lead to the formation of stacking faults and steps in the ITBs, results in detwinning or twin growth [23,27]. During the detwinning or twin growth process, CTBs were reported to be able to eliminate irradiation–induced defects [23,26,28]. As a result, the mobile CTBs have a larger territory to capture and annihilate the irradiation induced defects [26,27]. Thereby, the FCC γ–γ twinning structure in this study plays an important role on the suppression of the defect accumulation. For the HCP structure in this study, the SAED pattern of Fig. 4b shows that the parent lattice and twin lattice share the same $(1\bar{1}02)$ twinning plane, and orientational relationship between the parent lattice and twin lattice is the same as the conventional $\{10\bar{1}2\}$ twinning structure [29,30]. However, the HRTEM image in Fig. 4c shows that the ε–ε TB is composed predominantly of semicoherent basal–prismatic steps which lacks a crystallographic mirror relationship. Different from the movement of TBs of FCC crystal structure that is driven by collective glide of twinning dislocations under both irradiation condition and stress condition [23,27], migration of this special BP/PB steps undergoes a basal–prismatic transformation by atomic rearrangement under stress condition [17]. However, its behavior under irradiation environment is seldomly reported, which needs to be investigated in future study. Although the underlying mechanism of structural evolution of the ε–ε TB is unknown, as shown in Fig. 4, the special TB structure remains stable even up to a displacement damage of 50 dpa.

In HCP ε phase, the $\{0001\}\langle 11\bar{2}0\rangle$ is a commonly observed operative dislocation slip system, and in FCC γ phase, $\{111\}\langle 110\rangle$ is a preferred operative dislocation slip system. As it is shown in Fig. 5, the γ and ε phases have a standard S-N orientation relationship. When a partial dislocation with a Burger vector of $1/6\langle 11\bar{2}0\rangle$ operate in the $\{0001\}\langle 11\bar{2}0\rangle$ slip system in ε phase encounters the γ–ε interface, the dislocation will be impeded due to the discontinuity of operative dislocation slip system ($\{0001\}\langle 11\bar{2}0\rangle$ in ε phase VS $\{111\}\langle 110\rangle$ in γ phase), resulting in an improved strength of the DP–HEAs [15,31]. Moreover, as the material ductility is closely related with the number of possible operative dislocation slip systems, and the operative dislocation slip systems of FCC γ phase outnumber those of HCP ε phase. The γ phase in the DP–HEA serves as softer matrix to improve the overall ductility of the DP–HEAs. Above analysis indicates that the co–existence of γ–ε phases improve both strength and ductility of the DP–HEAs. TEM images in Fig. 5 show that the γ phase and ε phase co–existed and the orientational relationship between the two phases kept unchanged after irradiation, this proves that the γ–ε interfacial structure is stable under irradiation condition.

The above observations prove that the γ–γ, ε–ε twinning structures and the co–existed γ–ε dual phase structure in the $Fe_{50}Mn_{30}Co_{10}Cr_{10}$ DP–HEAs are stable under irradiation conditions at RT, indicating that the special microstructure induced by TWIP and TRIP mechanisms in the DP–HEAs still contributes to the improved strength and ductility under irradiation condition in a low temperature range.

SFE is an intrinsic property of the material that is closely related with the material chemical composition. Irradiation has been reported to reduce the SFE through the introduction of irradiation defects and microchemical segregation [32]. In this study, elemental segregation of the irradiated samples was not detected by energy dispersive spectroscopy (EDS) . Therefore, the high irradiation dose did not alter the chemical concentration, nor change the SFE (at least nor increase the SFE) . Moreover, with the decreasing of SFE, TWIP and TRIP mechanisms play a predominating role during the material deformation [33]. Therefore, based on the above results, the TWIP and TRIP mechanisms still work effectively and contribute to improve both strength and ductility of the DP–HEAs with low SFE under irradiation conditions in a low temperature range.

4.2. Defect free channels

Defect free channel is a form of plastic flow localization, it is formed by the glide of dislocation along slip planes. Passing dislocations sweep away or absorb defects until got pinned by stronger obstacles, leaving a defect free path, as a result, the subsequent dislocations can easily slip through the defect free pathways, pile up near the GBs, causes stress concentration and deformation localization [21,34]. Different from the previous findings that DFCs are formed by the sweeping of multiple mobile dislocations originating from grain boundaries or crack tips [21], recent study showed that irradiation induced dislocation loops could serve as dislocation sources that emit dislocations and initiate the defect free channels inside the grains [19]. As the dislocation loop is one of the most common defects in irradiated materials, the DFCs occur more readily in the irradiated materials. Once the DFCs formed, sustainable dislocations within the grains are not enough to provide necessary strain hardening [35], which finally lead to ductility loss and material failure.

DFCs are obvious in the I–T samples, as shown in the bright–field TEM image of Fig. 6a and the corresponding dark–field TEM

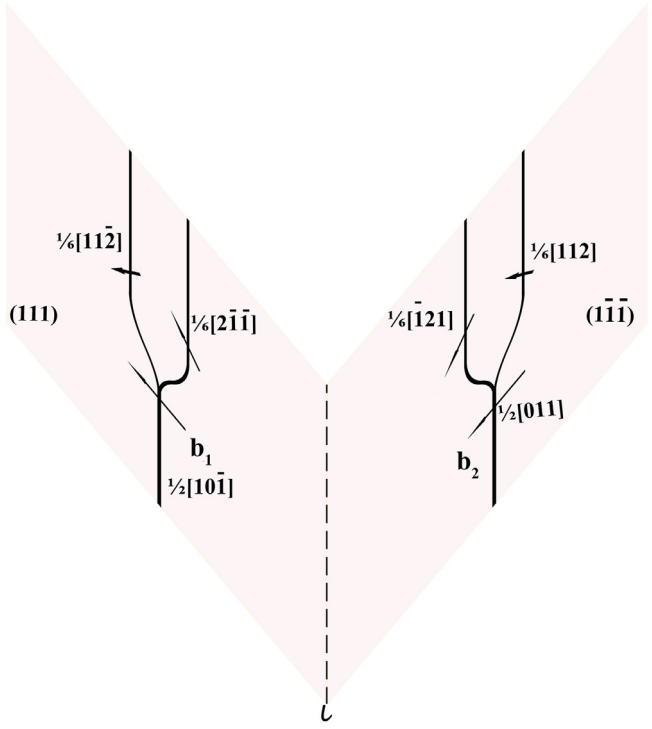

Fig. 7. Schematic diagram of the formation of L–C lock.

image of Fig. 6b. The most noteworthy feature is that numerous L–C locks locate at the edge of the DFCs as labeled by the yellow rectangles in Fig. 6a. L–C lock is a special type of sessile dislocation in FCC crystal structure [36]. Detail formation mechanism of L–C lock is shown schematically in Fig. 7. The perfect dislocation loops of $^1/_2[10\bar{1}]$ (with a burger vector of $\mathbf{b_1}$) in the close–packed plane (111) dissociate into $^1/_6[2\bar{1}\bar{1}]$ and $^1/_6[11\bar{2}]$ extended dislocations, as described in Eq. (1) . At the same time, perfect dislocation loops of $^1/_2[011]$ (with a burger vector of $\mathbf{b_2}$) in the close–packed plane $(1\bar{1}\bar{1})$ dissociate into $^1/_6[112]$ and $^1/_6[\bar{1}21]$ extended dislocations, as shown in Eq. (2) .

$$^1/_2[10\bar{1}] = {}^1/_6[2\bar{1}\bar{1}] + {}^1/_6[11\bar{2}] \tag{1}$$

$$^1/_2[011] = {}^1/_6[112] + {}^1/_6[\bar{1}21] \tag{2}$$

The extended dislocations of $^1/_6[\bar{1}21]$ and $^1/_6[2\bar{1}\bar{1}]$ glide in the close–packed planes of (111) and $(1\bar{1}\bar{1})$, respectively, until react with each other in the intersection line (ℓ) of the two close–packed planes following Eq. (3) . The resultant dislocation $^1/_6[110]$ (i.e. L–C lock) is a pure edge dislocation with a burger vector in (001) plane rather than in the close–packed plane of (111), as shown in Fig. 6c, therefore, it is energetically unfavorable to initiate the movement of $^1/_6[110]$.

$$^1/_6[\bar{1}21] + {}^1/_6[2\bar{1}\bar{1}] = {}^1/_6[110] \tag{3}$$

Above analysis shows that L–C locks are strong obstacles in FCC γ phase that block the propagation of mobile dislocations, decrease the mean free path of a dislocation. As discussed in detail in Ref. [37], $^1/_6[112]$ partial dislocations are preferentially formed in low SFE materials, according to Eq. (3), partial dislocations in {111} close–packed planes react with each other and result in the L–C locks. TEM images in Fig. 6 show that the resultant immobile L–C locks in grain interiors restrict the growth of DFCs, this will reduce the pile–up of dislocations along grain boundaries, and release stress concentration near grain boundaries.

5. Conclusions

The present work is part of an effect aimed at assessing the potential application of DP–HEA with low SFE serving as structural materials in the environment of nuclear energy systems. $Fe_{50}Mn_{30}Co_{10}Cr_{10}$ DP–HEA with characteristic of TWIP, B–TRIP effects and a low SFE of 6.5 mJ m^{-2} was chosen as the model material to be studied. Energetic Fe ions irradiation was employed to introduce displacement damage. TEM analysis found that, the γ–γ, ε–ε twinning structures and γ–ε co–existed structure, which are responsible for the good combination of high strength and high ductility of the DP–HEA, remain stable under a high irradiation dose (50 dpa) . Moreover, no elemental segregation induced by irradiation was detected by energy dispersive spectroscopy. Above results indicate that the TWIP and B–TRIP mechanisms are effective under irradiation condition at RT, and DP–HEAs possess the benefits brought by TWIP and B–TRIP mechanisms in improving both strength and ductility in irradiation environment in a low temperature range. DFCs and abundant L–C locks are observed in the irradiated–tensile samples. The low SFE of the DP–HEA contributes to the preferential formation of partial dislocations and the resultant L–C locks in this material. The L–C locks locate at the edges of DFCs and restrict the DFCs growth, which may finally reduce the pile–up of dislocations along grain boundaries, and release stress concentration near grain boundaries.

Author statement

Ji Wang: Conceptualization, Methodology, Investigation, Writing - original draft, Writing - review & editing, Visualization. Jianlong Chai: Methodology, Investigation, Visualization. Hongpeng Zhang: Investigation, Resources. Pengfei Tai: Methodology, Investigation, Resources. Chao Liu: Investigation, Resources. Lijuan Niu: Methodology. Wenhao He: Methodology. Weiying Huang: Methodology. Rui Shu: Investigation, Writing - original draft, Writing - review & editing. Laihui Luo: Conceptualization. Weiping Li: Conceptualization. Yabin Zhu: Conceptualization, Methodology, Writing - original draft, Resources, Supervision. Cunfeng Yao: Conceptualization, Methodology, Supervision, Funding acquisition. Peifeng Gao: Conceptualization, Methodology, Writing - review & editing, Funding acquisition, Supervision.

Declaration of Competing Interest

The authors declare that they have no known competing financial interests or personal relationships that could have appeared to influence the work reported in this paper.

Acknowledgements

This research was supported by the National Natural Science Foundation of China (Nos. 11902129, 11505247, U1832206 and U2032142), Strategic Priority Research Program of Chinese Academy of Sciences (No. XDA21010202), Natural Science Fund of Zhejiang Province (No. LQ20A050001), Natural Science Fund of Ningbo City (No. 2019A610183), and China Postdoctoral Science Foundation (2019T120963).

References

[1] B.S. Murty, J.W. Yeh, S. Ranganathan, High–Entropy Alloys, Elsevier, Netherlands, 2014.
[2] E.P. George, D. Raabe, R.O. Ritchie, Nat. Rev. Mater. 4 (2019) 515–534.
[3] M.H. Tsai, J.W. Yeh, Mater. Res. Lett. 2 (3) (2014) 107–123.
[4] D.S. Aidhy, C. Lu, K. Jin, et al., Acta Mater. 99 (2015) 69–76.
[5] F. Granberg, K. Nordlund, M.W. Ullah, et al., Phys. Rev. Lett. 116 (2016) 135504.
[6] C.Y. Lu, L.L. Niu, N.J. Chen, et al., Nat. Comm. 7 (2016) 13564.
[7] C.M. Barr, J.E. Nathaniel, K.A. Unocic, et al., Scr. Mater. 156 (2018) 80–84.

[8] C.Y. Li, X.X. Hu, T.F. Yang, et al., J. Nucl. Mater. 527 (15) (2019) 151838.
[9] A. Kareer, J.C. Waite, B. Li, et al., J. Nucl. Mater. 526 (1) (2019) 151744.
[10] T.F. Yang, S.Q. Xia, W. Guo, et al., Scr. Mater. 144 (2018) 31–35.
[11] T.F. Yang, W. Guo, J.D. Poplawsky, et al., Acta Mater. 188 (2020) 1–15.
[12] G. Ackland, Science 327 (2010) 1587–1588.
[13] I.J. Beyerlein, A. Caro, M.J. Demkowicz, et al., Mater. Today 16 (11) (2013) 443–449.
[14] W.J. Lu, C.H. Liebscher, G. Dehm, et al., Adv. Mater. 30 (44) (2018) 1804727.
[15] Z.M. Li, K.G. Pradeep, Y. Deng, et al., Nature 534 (2016) 227–230.
[16] B. Li, E. Ma, Phy. Rev. Lett. 103 (2009) 035503.
[17] B.Y. Liu, J. Wang, B. Li, et al., Nat. Comm. 5 (2014) 3297.
[18] H. Zhao, M. Song, S. Ni, et al., Acta Mater. 131 (2017) 271–279.
[19] S.H. Li, N. Gao, W.Z. Han, J. Mater. Sci. Tech. 58 (2020) 114–119.
[20] D. Kaoumi, V. Jammot, J. Nucl. Mater. 523 (2019) 33–42.
[21] J. Kacher, G.S. Liu, I.M. Robertson, Micron 43 (2012) 1099–1107.
[22] J. Wang, H. Huang, Appl. Phys. Lett. 88 (2006) 203112.
[23] J. Wang, N. Li, O. Anderoglu, X. Zhang, et al., Acta Mater. 58 (2010) 2262–2270.
[24] M.H. Yoo, J.K Lee, Philos. Mag. A 63 (5) (1991) 987–1000.
[25] K. Yu, D. Bufford, C. Sun, et al., Nat. Commun. 4 (2013) 1377.
[26] J. Li, D.Y. Xie, S. Xue, et al., Acta Mater. 151 (2018) 395–405.
[27] Y. Chen, H. Wang, M.A. Kirk, et al., Scr. Mater. 130 (2017) 37–41.
[28] W.Z. Han, M.J. Demkowicz, E.G. Fu, et al., Acta Mater. 60 (2012) 6341–6351.
[29] M. Yaghoobi, J.E. Allison, V. Sundararaghavan, Int. J. Plast. 127 (2020) 102653.
[30] A. Ostapovets, A.S. Gornakova, Mater. Lett. 247 (15) (2019) 99–101.
[31] D.H. Hong, T.W. Lee, S.H. Lim, et al., Scr. Mater. 69 (5) (2013) 405–408.
[32] J.P. Wharry, K.S. Mao, J. Mater. Res. 35 (13) (2020) 1–12.
[33] D.T. Pierce, J.A. Jiménez, J. Bentley, Acta Mater. 100 (2015) 178–190.
[34] T.D. Rubia, H.M. Zbib, T.A. Khraishi, et al., Nature 406 (2000) 871–874.
[35] J.H. Lee, T.B. Holland, A.K. Mukherjee, et al., Sci. Rep. 3 (2013) 1061.
[36] X.L. Wu, Y.T. Zhu, Y.G. Wei, et al., Phys. Rev. Lett. 103 (2009) 205504.
[37] V. Yamakov, D. Wolf, S.R. Philpot, et al., Nat. Mater 3 (2004) 43–47.